

Refereed, biannual scientific journal issued by: The Libyan Center for Solar Energy Research and Studies



Optoelectronic Properties of Doped CaTiO₃ (C, N, Si and P): A DFT Study for Photovoltaic Applications

Abdellah Bouzaid^{1*}, Younes Ziat², Hamza Belkhanchi³, Ayoub Koufi⁴, Mohammed Miri⁵, Hmad Fatihi⁶, Charaf Laghlimi⁷.

1,2,3,4,5 Engineering and Applied Physics Team (EAPT), Superior School of Technology, Sultan Moulay Slimane University, Beni Mellal, Morocco.
1,2,3,4,5,7 The Moroccan Asociation of Sciences and Techniques for Sustainable Development (MASTSD), Beni Mellal, Morocco.

⁶Laboratory of Research in Physics and Engineering Sciences, Sultan Moulay Slimane University, Polydisciplinary Faculty, Beni Mellal, 23000, Morocco.

⁷ERCI2A, FSTH, Abdelmalek Essaadi University, Tetouan, Morocco.

E-mail: ¹abdellah.bouzaid97@gmail.com.

SPECIAL ISSUE ON:

The 1st International Conference on Sciences and Techniques for Renewable Energy and the Environment. (STR2E 2025)

May 6-8, 2025 at FST-Al Hoceima-Morocco.

KEYWORDS

CaTiO₃; Ca₄ Ti₄ O₁₀ Y₂; DFT; Bulk modulus derivative; Band structure; electronic structure, optical properties.

ABSTRACT

This study uses density functional theory (DFT) with generalized gradient approximation (GGA) and modified Becke-Johnson potential (mBJ) to analyze the structural, electronic, and optical properties of Ca_4 $Ti_4 O_{(12-z_i)} Y_{zi}$ perovskite materials, where z_i indicates the number of dopant atoms at the oxygen (O) site. In this research, Y represents the elements C, N, Si, and P, which are substituted at oxygen sites with a doping concentration of x = 16%. Firstly, the structural optimization results reveal negative formation energies for both pure and doped $CaTiO_3$, confirming the stability.

Moreover, doping with Y significantly reduces the bandgap energy compared to undoped CaTiO₃ (2.766 eV). Specifically, the band gaps for Ca₄ Ti₄ O₁₀ Y₂ materials (Y = C, N, Si, and P) are reduced to 0.87, 1.63, 0, and 0.6 eV respectively. In addition, doping with C and N retains the nature of the indirect band gap, with electronic transitions between the Γ and L points of the Brillouin zone, whereas doping with P results in a direct band gap. Additionally, doping with Si reduces the band gap to zero, resulting in metallic behavior. Furthermore, the Fermi level (EF) shifts towards the valence band (VB), indicating p-type semiconductor behavior for the doped systems, except Ca₄ Ti₄ O10 Si₂, which exhibits metallic behavior. Finally, analysis of the optical properties shows that doping increases the static dielectric constant, ϵ_1 (0), with specific values

for each dopant 7.1 for Ca₄ Ti₄ O₁₀ C₂, 6.72 for Ca₄ Ti₄ O₁₀ N₂, 36.63 for Ca₄ Ti₄ O₁₀ Si₂, and 23.69 for Ca₄ Ti₄ O₁₀ P₂. Notably, doping CaTiO₃ with 16% of Y reduces the bandgap, improving optical absorption and conductivity in the visible range, making Ca₄ Ti₄ O₁₀ Y₂ (Y= C, N, Si, and P) a promising material for photovoltaic cells and optoelectronic applications.

الخصائص الضوئية والإلكترونية لمركب (Si ·N ·C وCaTiO المطعم: دراسة باستخدام نظرية الخصائص الوظيفة الكثيفة (DFT) للتطبيقات الكهروضوئية

عبد اللّه بوزايد، يونس زيات، حمزة بلخنشي، أيوب كوفي، محمد ميري، احمد فاتحي، شراف لغليمي.

ملغص: تستخدم هذه الدراسة نظرية الوظيفة الكثيفة (DFT) مع تقريب التدرج المعمم (GGA) وجهد بيك جونسون المعدل (mBJ) لتحليل الخصائص التركيبية والإلكترونية والبصرية لمواد البيروفسكاية إلى (P Sig N و Sig N كني يشير الإكسبيية والإلكترونية والبصرية لمواد البيروفسكاية الإكانية تحل محل الأكسبين عدد ذرات المنشطات في موقع الأكسبين (O). في هذا البحث، تمثل Y العناصر C و N Sig N و P التي تحل محل الأكسبين بتركيز تطعيم 16% على ذلك أولًا، تكشف نتائج تحسين البنية عن طاقات تكوين سالبة لكل من (CaTiO3 النقي والمطعم مما يؤكد استقرارهما. علاوة على ذلك، يقلل التطعيم ب Y بشكل كبير من طاقة فجوة النطاق مقارنة بو CaTiO3 غير المطعم (2.760 استقرارهما. على وجه التحديد، تنخفض فجوات النطاق لمواد Y و C و Ca4 Ti4 O10 كي حيث (Y = C, N, Si, P) إلى 7.80 و 1.03 و 1.03 و 1.03 و 1.04 و 1.03 و 1.03

الكلمات الفتاحية - DFT ؛ Ca4 Ti4 O₁₀ Y₂ ؛ CaTiO₃ ؛ مشتق معامل الكتلة؛ هيكل النطاق؛ البنية الإلكترونية والخصائص البصرية.

1. INTRODUCTION

The development of renewable energy solutions has become a major strategic issue on a global scale, given the current environmental and economic challenges. Renewable energy sources such as photovoltaics (PV), wind power and batteries offer promising prospects for meeting growing energy demand while limiting environmental impacts [1, 2, 3, 4]. These technologies not only help to reduce dependence on fossil fuels, but also promote sustainable development thanks to their economic, social and environmental benefits [5]. Identifying and harnessing renewable, sustainable and economically competitive energy sources is therefore a key priority in meeting the world's energy challenges [6].

Among the solutions being considered, solar energy occupies a central position due to its abundance, renewable nature and environmental friendliness. Its conversion into chemical energy via artificial photosynthesis represents an innovative and essential way of responding to the current energy and climate crises [6, 7, 8]. This process, inspired by nature, paves the way for revolutionary technologies capable of transforming the world's energy landscape over the long term. In this context, perovskite oxides, following the general formula ABO₃, stand out as cutting-edge materials. Their stable crystal structure, formed by the coordination of large (site A) and small (site B) cations with oxygen, gives them unique properties [9]. These versatile

materials have demonstrated their effectiveness in a wide range of technological applications, from photovoltaic devices and sensors to catalysts and energy storage systems [10, 11, 12, 13]. Their advantages include remarkable thermal stability, virtually unlimited lifetime, rapid charge cycles and excellent cost-effectiveness, positioning them as ideal candidates for meeting future energy needs [14]. In addition, perovskite-based ceramics have recently gained in popularity thanks to their structural adaptability, ease of synthesis and low cost. These materials offer an exceptional combination of properties, including high mechanical strength, low thermal expansion, modularity of physico-chemical properties, non-toxicity and high melting point [15]. These characteristics make ceramics particularly attractive solutions for demanding applications, reinforcing their potential in the energy transition. In this context, CaTiO₃ perovskite is attracting growing interest due to its remarkable photocatalytic properties, including its effectiveness in degrading organic pollutants and reducing carbon dioxide emissions through environmentally friendly methods [16, 17, 18]. In addition to its semiconducting properties, CaTiO₃ exhibits exceptional dielectric behavior, with a relative permittivity of up to 186 and a band gap of 3 to 4 eV, making it a particularly promising material for optoelectronic devices [19]. However, despite these assets, the photocatalytic performance of pure CaTiO₃ remains limited for hydrogen evolution due to its wide band gap of 3.5 eV, restricting its absorption to the ultraviolet region, which represents only around 5% of the solar spectrum [16, 20]. To overcome this limitation, advanced studies have explored strategies such as doping and nano structuring, aimed at improving its efficiency in photovoltaic and photocatalytic applications. The properties of CaTiO₃ are strongly influenced by a variety of factors, including crystalline defects at the A or B cation sites, particle size and morphology, and exposed surface area [21]. ATiO₃-type perovskite oxides (where A represents Ca, Ba, or Sr) are thus emerging as competitive materials for the next generation of solar cells and optoelectronic devices. These materials crystallize in tetragonal or cubic structures, where the A cations occupy the corners of the unit cell, the Ti cation is in the center, and the O anions are located at the edges of the cube [10, 22, 23]. Recent work also highlights the positive effect of doping on the performance of CaTiO₃. Attou et al. have, for example, used DFT to investigate the effects of boron (B) doping as a replacement for oxygen sites. Their results show that this doping reduces the bandgap, improves visible light absorption, and optimizes optical and transport properties, particularly in the energy range from 2 to 4 eV [24]. In addition, (La-S) doping with a ratio of 0.25 demonstrated a notable improvement in photocatalytic hydrolysis, thanks to a narrower bandgap, improved carrier mobility and enhanced absorption of visible light [17]. Other studies have revealed that Sr doping alters the electronic band structure of CaTiO₃. This doping initially increases the band gap, but at higher concentrations it decreases, paving the way for fine-tuning of optical and electronic properties [25]. This study focuses on analyzing the structural, electrical, and optical properties of the material CaTiO₃ doped with a precise 16% concentration of various doping elements, including carbon (C), nitrogen (N), silicon (Si), and phosphorus (P), using simulations based on density functional theory (DFT). This choice of concentration was carefully selected to optimize the interaction of the dopants with the host structure while minimizing crystal defects that could affect the overall stability of the material. The use of DFT provides a rigorous theoretical framework for examining dopinginduced modifications to the fundamental properties of CaTiO₃, such as lattice parameters, electron density, and band structure. In particular, the aim is to assess how each type of dopant influences the band gap, which is essential for applications in photocatalysis and optoelectronic devices. In addition, this approach makes it possible to investigate changes in optical response, such as absorption and extinction coefficients, as well as electrical properties such as charge carrier mobility and conductivity. This research, combining advanced simulations and predictive analyses, will contribute to a broader understanding of the fundamental mechanisms involved in doping CaTiO₃. They will also provide avenues for designing innovative materials with tuned properties, meeting the specific needs of renewable energy technologies and next-generation optoelectronic devices.

2. COMPUTATIONAL METHOD

This study explored the structural, electronic, and optical properties of cubic CaTiO₃ perovskites, both in their pure state and doped with elements C, N, Si, and P, at a specific concentration of 16%. The research relies on the full-potential linearized augmented plane wave (FP-LAPW) method, integrated into the WIEN2k code, to solve the Kohn-Sham equation within the framework of DFT [26, 27]. To ensure greater accuracy, the GGA approximation was combined with the mBJ approximation, known to provide bandgap estimates consistent with experimental results [28, 29]. CaTiO₃ perovskites adopt a cubic structure characterized by the space group Pm3m (no. 221). In this configuration, the Ca and Ti cations occupy positions (0, 0, 0) and (1/2, 1/2, 1/2) respectively within the unit cell, while the oxygen anions are located at positions (0, 1/2, 1/2), (1/2, 0, 1/2) and (1/2, 1/2, 0), thus forming tetrahedra and octahedra around the cations. Simulation parameters include a cut-off value Rmt* Kmax = 7, where Kmax is the maximum magnitude of the K vector, and Kmax represents the smallest radius of the atomic sphere of the unit cell and Rmt Muffin-Tin Radii (see Table 1).

Table 1: Muffin-Tin Radii (RMT) for pure and doped Ca₄Ti₄ O₁₀ Y₂ (Y= C, N, Si, and P) perovskites.

Element	Ca	Ti	0	С	N	Si	P
RMT (a.u.)	2.5	1.92	1.74	1.64	1.69	1.74	1.74

These parameters guarantee the convergence of the basis set used for the calculations. The convergence criteria have been defined with a tolerance of 10-5 Ry for energy and 10-4 e for charge. For optimization, a k-mesh of $10\times10\times10$ was used for Brillouin zone sampling, and the central state charge localization was established with a value of -6 Rydberg. To model the effects of doping, a $2\times2\times1$ supercell of pure CaTiO₃ was constructed, comprising 4 Ca atoms, 4 Ti atoms, and 12 oxygen atoms. In this model, some oxygen sites were replaced by doping elements (C, N, Si, and P) at a concentration of 16%. This approach enables accurate simulation of dopant-host interactions. Figure 1(a) illustrates the CaTiO₃ unit cell, composed of one Ca atom, one Ti atom, and three oxygen atoms.

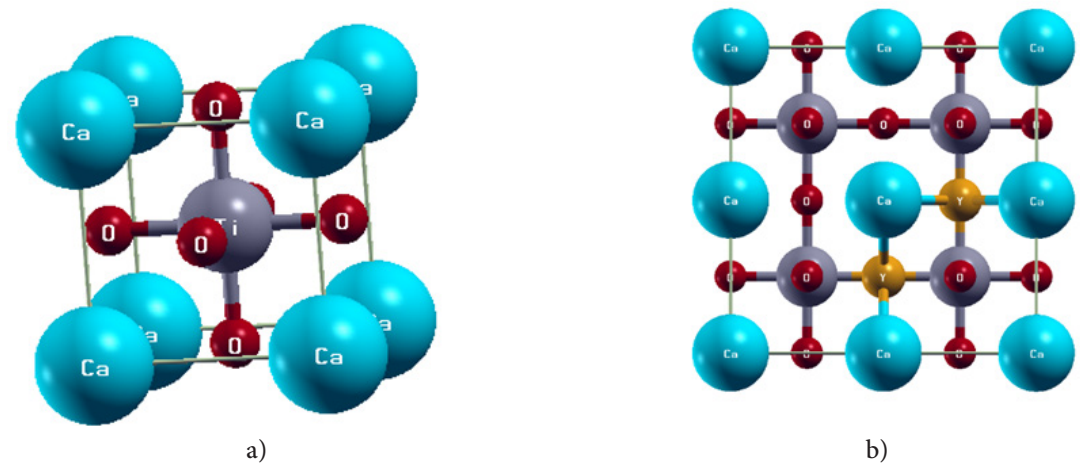


Figure 1: Crystal Structure of CaTiO₃: (a) unit cell and (b) 2*2*1 supercell.

Figure 1(b) shows the $2\times2\times1$ supercell, consisting of 4-unit cells arranged in a 2×2 grid along axes a and b, while axis c axis remains unchanged, reproducing a doping concentration of 16%.

In this arrangement, Ca cations occupy the central positions of the octahedra, with each Ti cation surrounded by six tilted oxygen anions. This structure enables us to explore in detail the impact of doping on the crystal structure, electron density, and optical properties of the material. These results will contribute to a better understanding of the fundamental mechanisms and optimize the properties of perovskites for advanced applications in optoelectronic devices and energy technologies.

3. RESULTS AND DISCUSSIONS

3.1. Properties Structural and formation energy:

The Birch-Murnaghan equation of state is used to optimize the volume and determine the equilibrium lattice parameters, considering the pressure derivative of the bulk modulus [30]:

$$\boldsymbol{E}_{tot} = \boldsymbol{E}_{0} + \frac{9\boldsymbol{V}_{0}\boldsymbol{B}}{16} \left\{ \left[\left(\frac{\boldsymbol{V}_{0}}{\boldsymbol{V}} \right)^{2/3} - 1 \right]^{2} B' + \left[\left(\frac{\boldsymbol{V}_{0}}{\boldsymbol{V}} \right)^{2/3} - 1 \right] \left[6 - 4 \left(\frac{\boldsymbol{V}_{0}}{\boldsymbol{V}} \right)^{2/3} \right] \right\}$$
(1)

Where E denotes the total energy of the material, E_0 is the ground state energy at zero pressure, V represents the volume, V_0 is the equilibrium volume, B is the bulk modulus, and B' is the pressure derivative of the bulk modulus [31].

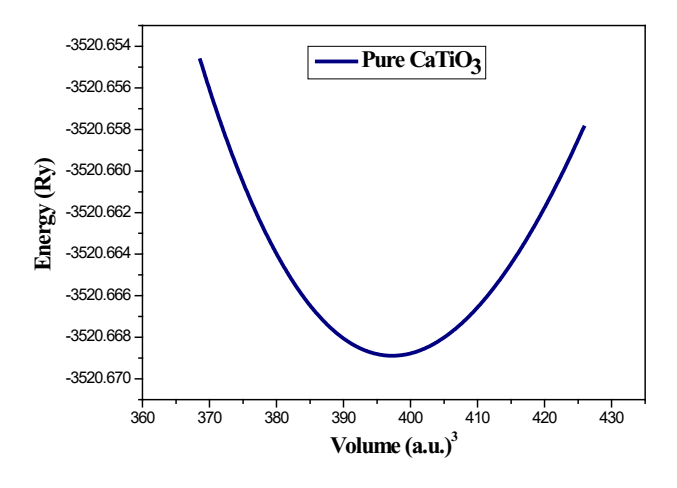


Figure 2: Total energy variation of CaTiO₃ as a function of volume.

Table 2: Properties of pure CaTiO₃ compounds, such as bulk modulus, lattice constant, and bulk modulus derivatives.

Parameter	Our work	other study	
Lattice constant (Å)	3.8901	3.899 [17]	
		3.856 [9]	
Bulk modulus (GPa)	177.4884	200.598 [9]	
Bulk modulus derivative	4.2350	5.046 [9]	
Volume (a.u)3	397.2763	386.846 [9]	

Figure 2 shows the volume optimization curve of total energy against the volume of pure CaTiO₃. The optimized lattice parameters of pure CaTiO₃ $a_0 = b_0 = c_0 = 3.89$ Å were consistent with both experimental findings ($a_0 = 3.8967$ [32] and 3.90 Å [33]) and theoretical data ($a_0 = 3.899$ [17], and 3.856 Å [9]). Table 2 presents the relaxed lattice constants, bulk modulus, bulk modulus derivative, volume, and ground-state energy of the pure CaTiO₃ compound in its optimized

structure. The ground state derived from the optimization curve, based on the lattice parameter, is used to calculate the electronic and optical properties of the compounds self-consistently. A negative formation energy reflects the thermodynamic stability of the compound compared to its constituent elements [34, 35, 36]. In this study, the formation energy was calculated to assess the thermodynamic stability of the material. The negative formation energy value for CaTiO₃, which is -3.33 eV/atom, clearly indicates its thermodynamic stability. The computation of defect formation energy allows inferring the experimental growth potential of a material. A lower formation energy makes the doping structure easier and more stable [37, 38]. The following formula is used to determine the defect production energy of the doped materials [39, 40, 41]:

$$\Delta E_f = (\mathbf{E}_{Y-doped} - \mathbf{E}_{undoped}) + z_i(\mu_o - \mu_Y)$$
 (2)

Where $E_{Y\text{-}doped}$ and $E_{undoped}$ are the total energies of the supercell with and without the dopant, μ_O and μ_Y (Y = C, N, Si, P) are the chemical potentials of oxygen and the dopants, z_i is the number of dopant atoms. Table 3 shows that doping reduces the Formation energy, improving the material's thermodynamic stability.

Table 3: Formation energy of pure CaTiO₃ and dopedCa₄Ti₄ O₁₀ Y₂ (Y= C, N, Si, and P).

Compounds	CaTiO₃	Ca ₄ Ti ₄ O ₁₀ C ₂	Ca ₄ Ti ₄ O ₁₀ N ₂	Ca ₄ Ti ₄ O ₁₀ Si ₂	Ca ₄ Ti ₄ O ₁₀ P ₂
Ef(eV/atom)	-3.33	-34.2856492	-41.9969731	-38.9171817	-33.9392253

3.2. Electronic properties:

Calculations based on DFT were carried out to analyze the electronic properties of pure CaTiO₃ and dopedCa₄Ti₄ O₁₀ Y₂(Y= C, N, Si, and P). These calculations revealed the changes made to the electronic structure of CaTiO₃ as a result of doping. Figure 3 (a, b, c, d, and e) shows the energy band structures of the various compounds, in the energy range from -5 to 8 eV. The bandgap diagrams of the compounds are plotted along the high-symmetry path (W-L- Γ -X-W-K) in the Brillouin zone for a cubic structure, with the Fermi energy level (E_t) aligned at zero.

For pure CaTiO₃ (Figure 3 (a)), an indirect bandgap is observed between the L and Γ points. The bandgap width, calculated via the GGA approximation, is estimated at 2.003 eV. However, the use of the mBJ potential improves this estimate to 2.766 eV, reducing the discrepancy with the experimental value measured at 3.46 eV [42]. This refinement corrects the underestimation typical of standard GGA calculations and validates the increased accuracy offered by the mBJ potential. Furthermore, the general characteristics of the band structure and shift trends remain consistent with previous studies [9, 40]. InCa₄Ti₄ O₁₀ Y₂ (Y= C, N, Si, and P) produces subtle but significant changes in the bandgap. In general, doping with elements having a lower electronegativity than oxygen increases the valence band maximum (VB) while stabilizing the conduction band minimum (CBM) [40] . This interaction results in a slight narrowing of the band gap. Doped compounds exhibit similar electronic behavior, marked by electron transitions from the valence band (VB) to the conduction band (CB). Doping also induces the formation of new electronic energy levels within the band gap. These intermediate levels facilitate electronic transitions between the VB and CB, thereby improving the overall electronic properties of the material. More specifically, compounds doping with Y (C, N) result in the valence band maxima (VBM) and conduction band minima (CBM) being located at L and Γ points, respectively, indicating indirect band gap energy. In contrast, doping with P results in both the VBM and CBM being situated at the high-symmetry point Γ , indicating a direct band gap. In contrast, doping with silicon results in a complete overlap between the VB and the CB, effectively reducing the band gap to zero. As a consequence, the materials studied exhibit conductive properties.

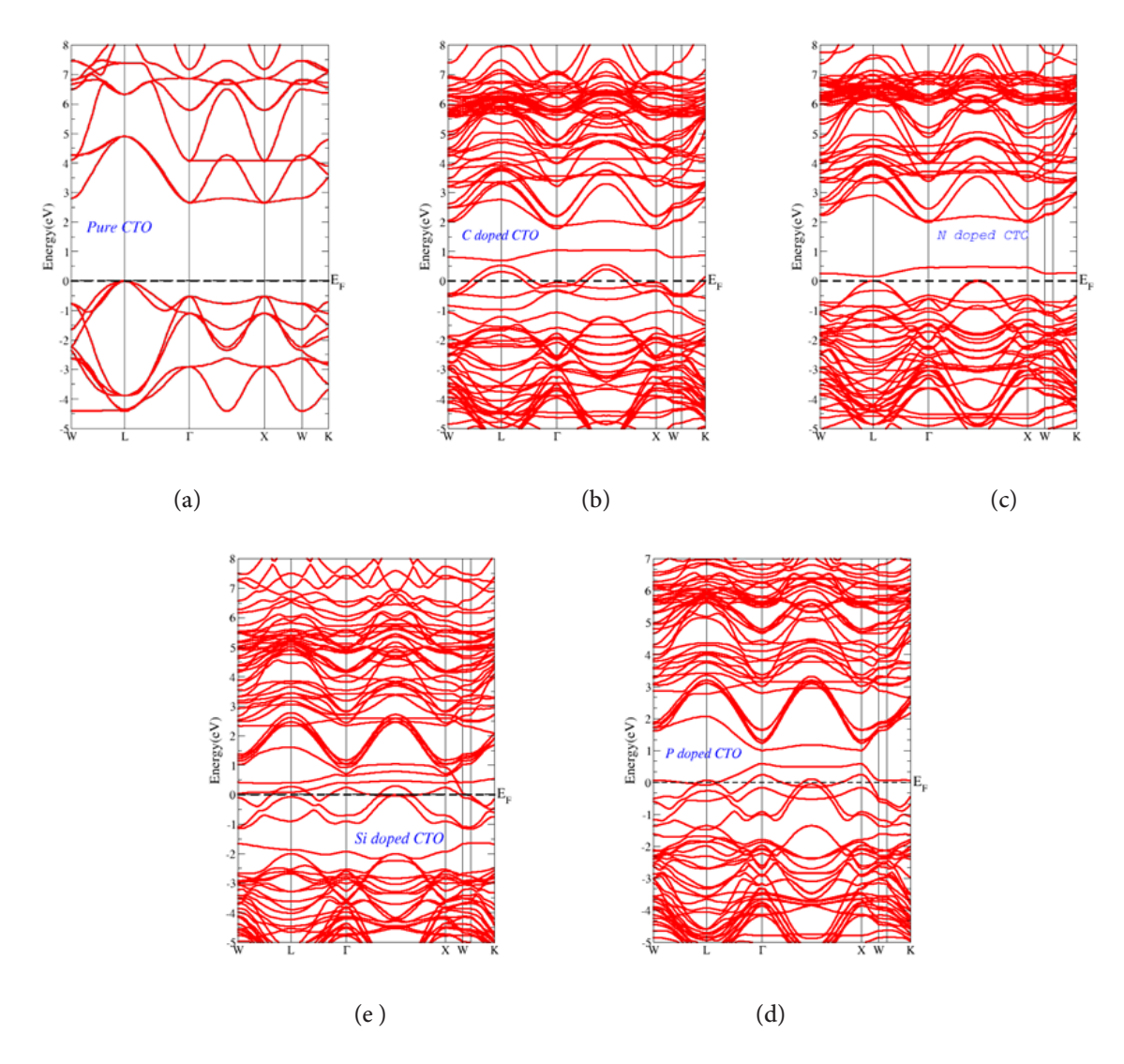
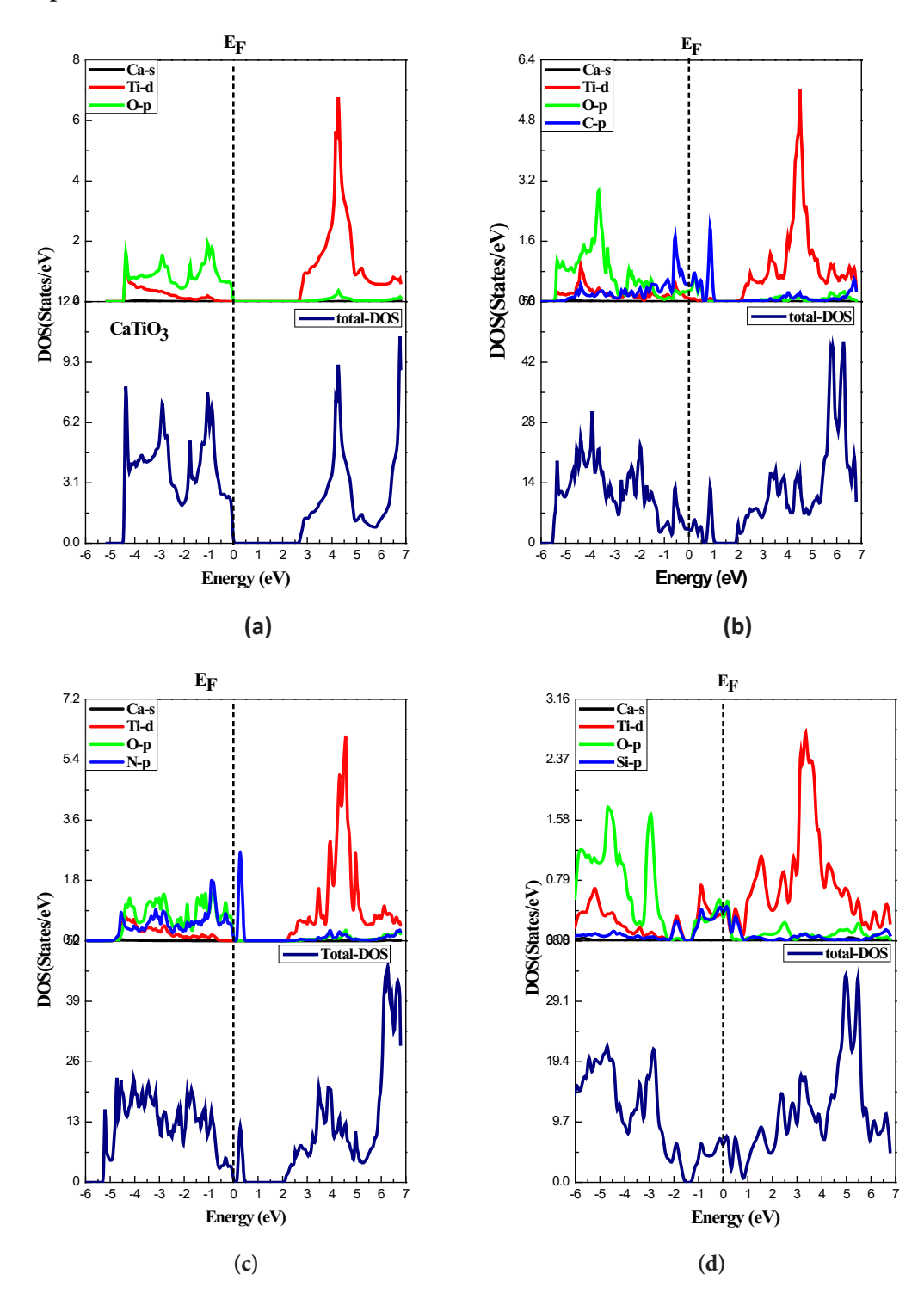


Figure 3: Band structure of (a) CaTiO₃, (b) Ca₄Ti₄O₁₀C₂, (c) Ca₄Ti₄O₁₀N₂, (d)Ca₄Ti₄O₁₀Si₂, and (e) Ca₄Ti₄O₁₀P₂.

Density of states (DOS) analysis provides crucial information on the electronic properties and chemical interactions of solid materials. In this study, the total DOS (TDOS) of pure CaTiO₃ and doped Ca₄Ti₄O₁₀Y₂ (Y= C, N, Si, and P) has been examined to assess the impact of doping on its electronic properties. The calculations, carried out after full relaxation of the crystal structures using the GGA+mBJ potential, cover an energy range from -6 eV to 7 eV, with the Fermi level fixed at 0 eV. For pure CaTiO₃, the electronic contribution is dominated by the hybridized O-2p, Ca-4s, and Ti-3d orbitals. The O-2p orbitals, located close to the Fermi level, play a decisive role by contributing a significant number of electrons. The lowest unoccupied band is dominated by Ti-3d orbitals, reflecting the intrinsic electronic nature of the material (Figure 4(a)). In doped structures, significant changes are observed in the DOS (Figures 4(b, c, d and e)), particularly at the bandgap level. Measured bandgap widths are 0.87 eV for Ca₄Ti₄O₁₀C₂ 1.63 eV for Ca₄Ti₄O₁₀N₂, 0 eV for Ca₄Ti₄O₁₀Si₂ and 0.6 eV for Ca₄Ti₄O₁₀P₂.

Furthermore, these results reveal a significant bandgap decrease in all doped compounds. In particular, Si doping reduces the band gap to zero, giving the material a metallic behavior. However, the movement of the Fermi level toward the VB in doped materials signifies p-type SC behavior. This reflects an increase in the concentration of hole carriers, which could improve performance in applications requiring p-type conductivity, such as electronic and optoelectronic devices. In

conclusion, this study demonstrates that doping $Ca_4Ti_4O_{10}Y_2$ (Y= C, N, Si, and P) substantially modifies its electronic properties. These results highlight the potential of this material to be tuned for specific applications, ranging from semiconductors to metallic conductors, depending on the dopant used.



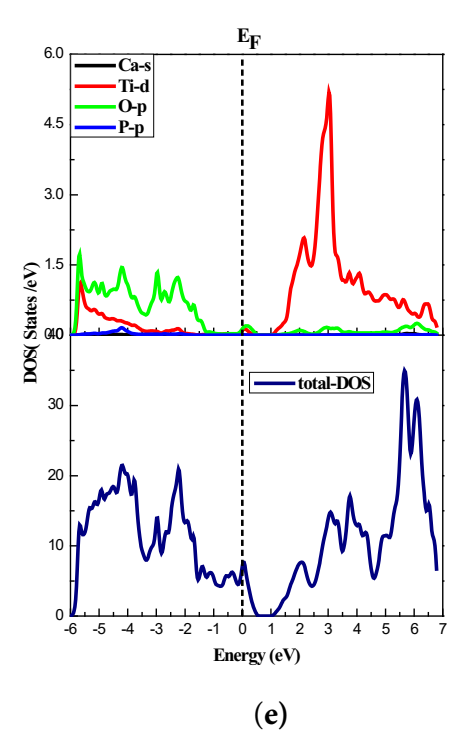


Figure 4: TDOS and PDOS for (a) CaTiO₃, (b)Ca₄Ti₄ O₁₀ C₂, (c) Ca₄Ti₄ O₁₀ N₂, (d)Ca₄Ti₄ O₁₀Si₂, and (e)Ca₄Ti₄ O₁₀ P₂.

3.3. Optical properties

The optical properties of pure CaTiO₃ and dopedCa₄Ti₄O₁₀Y₂ (Y= C, N, Si, and P) have been studied to assess the impact of dopants on their electronic structure. These properties include dielectric functions (real part, $\varepsilon_1(\omega)$, and imaginary part, $\varepsilon_2(\omega)$), absorption coefficient, $\alpha(\omega)$, and optical conductivity, $\sigma(\omega)$.

The dielectric function ε (ω) was computed [43, 44, 45]:

$$\varepsilon(\omega) = \varepsilon_1(\omega) + i\varepsilon_2(\omega) \tag{3}$$

The dielectric function real part ($\varepsilon 1(\omega)$) is obtained through the Kramers-Kronig transformation [46, 47]:

$$\varepsilon_{1}(\omega) = 1 + \frac{2}{\pi} P \int \frac{\omega' \, \varepsilon_{2}(\omega')}{\left({\omega'}^{2} - \omega_{12}\right)} d\omega' \tag{4}$$

The imaginary part $(\varepsilon_2(\omega))$ values are calculated using the following procedure [48, 49, 50]:

$$\varepsilon_{2}(\omega) = \left(\frac{4\pi^{2}e^{2}}{m^{2}\omega^{2}}\right) \sum_{i,j} i \left| M \right| j^{2} f_{i} \left(1 - f_{j}\right) \delta\left(E_{f} - E_{i} - \omega\right) d^{3} K \tag{5}$$

The element of the dipole matrix is denoted M, the electron mass is m, the elementary charge is e, and P represents the principal value of the integral in this context. The initial and final states are denoted by the indices i and j respectively. The energy of the electron in state i, with wave vector k, is denoted by E_i , and the Fermi-Dirac distribution function associated with state i is denoted by f_i .

The $\varepsilon_1(\omega)$ and $\varepsilon_2(\omega)$ components enable the determination of various optical properties, such as the absorption coefficient $\alpha(\omega)$, using the following formula [48, 51, 52]:

$$\alpha(\omega) = \sqrt{2}\omega \left[\sqrt{\varepsilon_1(\omega)^2 + \varepsilon_2(\omega)^2} - \varepsilon_1(\omega) \right]^{1/2}$$
 (6)

The optical conductivity is calculated using the relationship that follows [48, 53]:

$$\sigma(\omega) = \frac{\omega}{4\pi} \varepsilon_2(\omega) \tag{7}$$

• Dielectric function

Figure 5(a) shows the variation of $\varepsilon_1(\omega)$ for pure and doped CaTiO₃, in an energy range from 0 to 14 eV. This function describes the material's response to an electric field, in particular its ability to polarize and store electrical energy. The static dielectric constant, $\varepsilon_1(0)$, which reflects polarization at low frequencies, shows a significant increase after doping. For pure CaTiO₃, $\varepsilon_1(0)$ is 4.25. However, when doped at a concentration of x = 16%, the values of $\varepsilon_1(0)$ increase to 7.1 $for Ca_4 Ti_4 O_{10} C_2$, 6.72 for $Ca_4 Ti_4 O_{10} N_2$, 36.63 for $Ca_4 Ti_4 O_{10} Si_2$, and 23.69 for $Ca_4 Ti_4 O_{10} P_2$. This trend indicates that the introduction of dopants enhances the material's polarizability. The observed increase in $\varepsilon_1(0)$ can be attributed to the dopants' ability to induce additional dipoles, alter both ionic and electronic polarizability, and modify the local electronic structure, thereby amplifying the dielectric response of the material [54]. At low energy, all dopants increase the material's polarizing strength, thereby decreasing its overall polarization. The arrangement of dopants by polarizing strength follows this order: Si > P > C > N > pure CaTiO₃. This indicates that Si is the most effective dopant for enhancing the material's dielectric response, as it has the greatest impact on polarization. In the high-energy range of 8 to 13 eV, the dielectric function becomes negative for both the pure and Y-doped materials, indicating that reflection is the dominant mechanism in this region [54]. Furthermore, the $\varepsilon_1(\omega)$ of the dielectric function's negative values indicate that the electromagnetic wave is dampened, and zero values suggest that longitudinally polarized waves may exist [55].

The $\varepsilon_2(\omega)$, is a key parameter for understanding electronic absorption processes in materials. Figure 5(b) illustrates $\varepsilon_2(\omega)$ for pure and doped CaTiO₃ in an energy range from 0 to 14 eV. The optical spectrum highlights several distinct peaks, associated with interband transitions between valence and conduction bands. Pure CaTiO₃, the absorption threshold is identified at around 2.766 eV, corresponding to electronic transitions involving the Ca-s, O-2p, and Ti-3d orbitals of the VB, and the Ti-3d and O-2p orbitals of the CB. An increase in $\varepsilon_2(\omega)$ is observed with photon energy, culminating in a notable peak around 4.88 eV. The latter is attributed to marked transitions between the Ti-3d and O-2p orbitals, which play a decisive role in the optical properties of CaTiO₃. Moreover, the presence of peaks within the visible spectrum indicates enhanced light absorption in this range, making CaTiO₃ a promising material for applications in optoelectronics [56]. Farther, Si- and P-doped structures show low-energy absorption thresholds (P₁, P₂) between 0 and 0.5 eV, indicating in-band transitions from occupied states near the valence band to Si-p and P-p acceptor states just below the E_f . These transitions suggest that electronic excitations from the valence band happen at lower energies, which enhances electrical conductivity by increasing hole concentration compared to the pure structure. The Ca₄Ti₄O₁₀ Y₂(Y = C, N, Si, and P) notably alters its optical properties, shifting the absorption peaks to lower energies at approximately 2.60, 1.84, 2.27, and 3.20 eV, respectively. These peaks, associated with the $\varepsilon_2(\omega)$, indicate the material's electronic absorption and enhance its visibility within the spectrum. Furthermore, Ca₄Ti₄O₁₀Y₂ (Y = C, N, Si, and P) improves absorption in the visible range, making these compounds ideal for technological applications, especially in photovoltaics and optoelectronics [56].

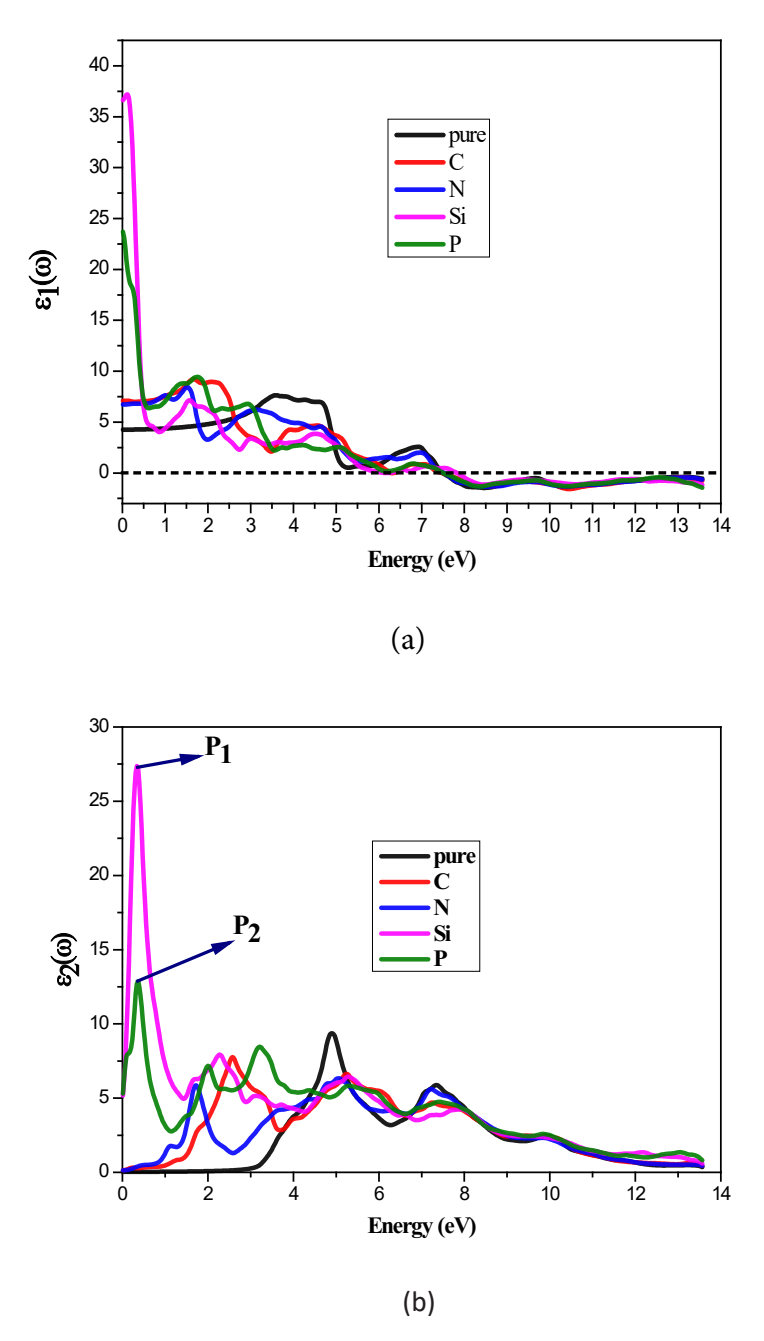


Figure 5: Dielectric function of pure CaTiO₃ and doped Ca₄Ti₄O₁₀Y₂ (Y= C, N, Si, and P): (a) Real part, (b) Imaginary part.

Absorption coefficient

To maximize the efficiency of photovoltaic systems and fully exploit the solar spectrum, it is crucial to incorporate materials with strong absorption properties in the visible range (400-800 nm) [56, 57]. Optical absorption occurs when the energy of incident photons ($E = h\nu$) exceeds the energy of the band gap, allowing the excitation of electrons from the VB to the CB, thus generating a photovoltaic effect [57].

Figure 6 illustrates the absorption coefficient $\alpha(\omega)$ of pure and doped CaTiO₃ in an energy range from 0 to 14 eV. It clearly appears that doping with chalcogen elements significantly enhances absorption in the visible range, with absorption coefficients reaching values as high as 104 cm⁻¹. This enhancement of absorption in the visible is attributed to the bandgap narrowing observed in

 $Ca_4Ti_4O_{10}Y_2$ (Y = C, N, Si, and P). Notably, when the material is doped with 16% of Y and elements such as C, N, Si, and P, its absorption properties in this spectral range are significantly enhanced, demonstrating its potential as a promising material for photovoltaic cells and optoelectronic devices.

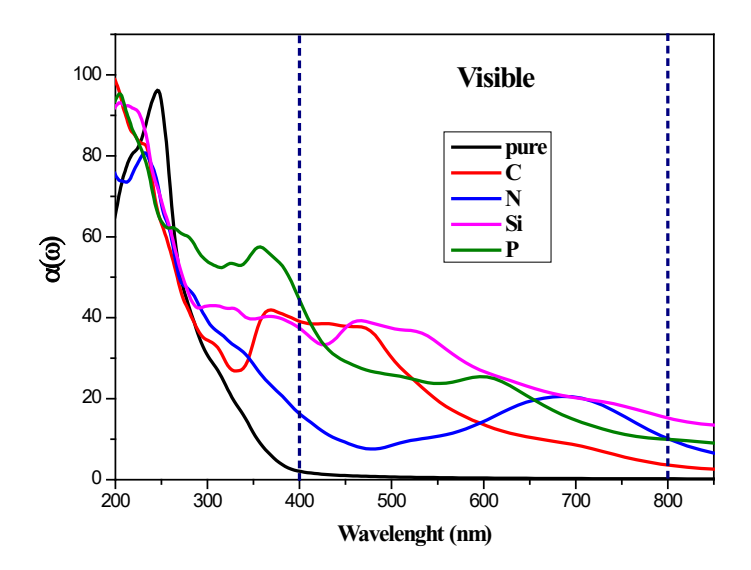


Figure 6: Absorption coefficient for pure CaTiO₃ and doped Ca₄Ti₄ O₁₀ Y₂ (Y= C, N, Si, and P).

• Optical conductivity

Figure 7 illustrates $\sigma(\omega)$ for pure CaTiO₃ and doped Ca₄Ti₄O₁₀Y₂(Y=C, N, Si, and P) over an energy range of 0 to 14 eV, which represents the material's ability to transport electrons in response to an applied electromagnetic field [58]. For pure CaTiO₃, the $\sigma(\omega)$ curve reveals a threshold energy of 2.76 eV, marking the band edge associated with electronic transitions from O-2p to Ti-3d states near the VBM. This threshold indicates that indirect transitions primarily occur along the (Γ -L) directions in the Brillouin zone, reflecting electron movements through the crystal structure. The substituting Y dopants (Y= C, N, Si, and P) greatly enhance optical conductivity over a broad energy range, indicating better semiconducting properties and increased charge carrier mobility.

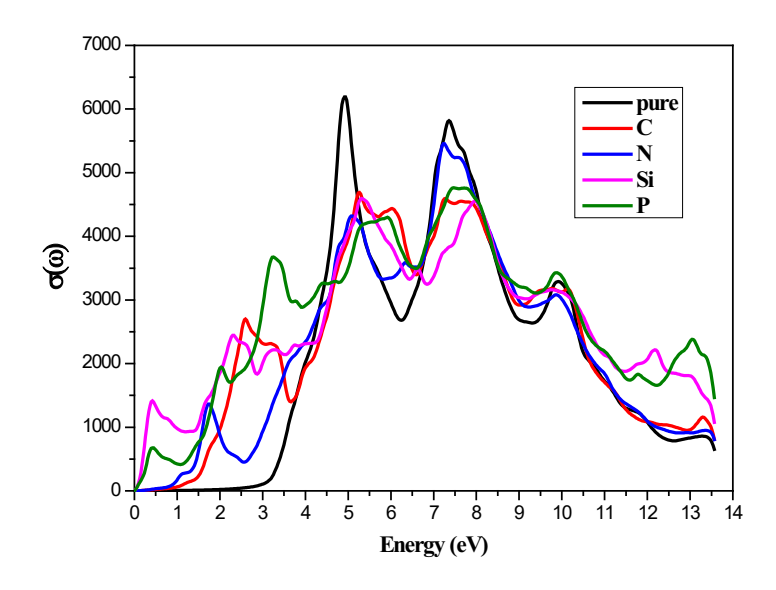


Figure 7: Optical conductivity for pure CaTiO₃ and doped Ca₄Ti₄O₁₀Y₂ (Y= C, N, Si, and P).

Distinct peaks in the $\sigma(\omega)$ curves for the doped compounds highlight enhanced excitation, demonstrating the effectiveness of substitutional doping in improving conductivity. Additionally, some peaks are observed in the visible range for MgTiO₃ doped with Y (C, N, Si, P), which may clarify the close relationship between the $\alpha(\omega)$ and $\sigma(\omega)$. Further, the presence of peaks in the visible range indicates improved light absorption, which is beneficial for photocatalytic and optoelectronic applications. The maximum conductivity values for C, N, Si, and P doping are 4651.01, 5423.62, 4656.04, and 4748.27 Ω^{-1} cm⁻¹, respectively. This enhancement is due to the introduction of new electronic states from the dopants, which improve photon absorption, excitation capacity, and electron mobility, thereby optimizing the material's semiconducting performance. In conclusion, the analysis of $\sigma(\omega)$ shows that doping Ca₄ Ti₄ O₁₀Y₂(Y= C, N, Si, and P) is promising for advanced applications like photovoltaic and optoelectronic devices, where enhanced optical conductivity and tunable light absorption are essential for optimal performance.

4. CONCLUSION

This study explores in detail the structural, electronic and optical properties of the perovskite compound CaTiO₃, both in its pure form and doped with halogen elements such as C, N, Si and P. Using ab initio calculations based on the FP-LAPW approach within the framework of DFT via the Wien2k code and the GGA-mBJ approximation, we have demonstrated that pure CaTiO₃ has an indirect band gap of 2.766 eV, which indicates its semiconductor properties. Further, compounds doped with Y (C, N) exhibit an indirect band gap, whereas doping with P results in a direct band gap. Additionally, doping with Si reduces the band gap to zero. DOS reveals that the introduction of Y shifts the EF towards the VB, which is typical of p-type SC and reduces the bandgap width. The results also show that bandgap values decrease with increasing dopant concentrations: 0.87 eV for Ca₄Ti₄O₁₀C₂, 1.63 eV for Ca₄Ti₄O₁₀N₂, 0 eV for Ca₄Ti₄O₁₀Si₂ and 0.6 eV for $Ca_4Ti_4O_{10}P_2$. Concerning optical properties, doping influences optical conductivity $\sigma(\Omega)$, with maximum values of 4651.01, 5423.62, 4656.04, and 4748.27 Ω^{-1} cm⁻¹ respectively for the elements C, N, Si, and P. These results indicate a significant improvement in the optical properties of the material. Notably, $Ca_4Ti_4O_{10}Y_2(Y=C, N, Si, and P)$ leads to a decrease in the bandgap, promoting absorption in the visible range and increasing optical conductivity. These improvements position Y-doped CaTiO₃ as a promising material for applications in photovoltaic cells and optoelectronic devices. In summary, this study highlights the crucial impact of doping on the electronic and optical properties of CaTiO₃, offering interesting prospects for using this material in renewable energy conversion technologies and next-generation optoelectronic devices.

Authors contribution: Abdellah Bouzaid: Writing – original draft, Visualization, Validation, Investigation, Formal analysis, Data curation, Conceptualization. Younes Ziat: Supervision. Hamza Belkhanchi: Visualization, Validation, Investigation, Formal analysis. Ayoub Koufi: Visualization. Mohammed Miri: Visualization. Hmad Fatihi: Visualization. Charaf Laghlimi: Visualization and validation. The author also reviewed and edited the manuscript for final approval.

Funding: The authors are warmly grateful to the support of "The Moroccan Association of Sciences and Techniques for Sustainable Development (MASTSD), Beni Mellal, Morocco". **Data Availability Statement:** Not applicable.

Conflicts of Interest: The authors declare that they have no conflict of interest.

Acknowledgements: A deep thanks to Ms Saloua Rzaoudi, Miss Khadija Ziat and Miss Amina Ziat for their support. A special thank you to Professor Hanane Reddad from Sultan Moulay Slimane University, Beni Mellal, Morocco, for her technical and scientific support, as well as her full collaboration and discussion during the different steps of the present investigation.

REFERENCES

- [1] A. Koufi, Y. Ziat, H. Belkhanchi, M. Miri, N. Lakouari, & F. Z. Baghli. A computational study of the structural and thermal conduct of MgCrH3 and MgFeH3 perovskite-type hydrides: FP-LAPW and BoltzTraP insight., E3S Web of Conferences (Vol. 582, p. 02003), 2024. https://doi.org/10.1051/e3sconf/202458202003
- [2] A. Raihan, J. Rahman, T. Tanchangtya, M. Ridwan, & S. Islam. An overview of the recent development and prospects of renewable energy in Italy. Renewable and Sustainable Energy, 2(2), 0008 (2024).
- [3] D. Gayen, R. Chatterjee, & S. Roy. A review on environmental impacts of renewable energy for sustainable development. International Journal of Environmental Science and Technology, 21(5), 5285-5310 (2024).
- [4] U. M. Adanma, & E. O. Ogunbiyi. Assessing the economic and environmental impacts of renewable energy adoption across different global regions. Engineering Science & Technology Journal, 5(5), 1767-1793 (2024).
- [5] C. Acar, I. Dincer, & G. F. Naterer. Review of photocatalytic water-splitting methods for sustainable hydrogen production. International Journal of Energy Research, 40(11), 1449-1473 (2016).
- [6] S. Du, & F. Zhang. General applications of density functional theory in photocatalysis. Chinese Journal of Catalysis, 61, 1-36 (2024).
- [7] W. Tu, Y. Zhou, & Z. Zou. Photocatalytic conversion of CO2 into renewable hydrocarbon fuels: state-of-the-art accomplishment, challenges, and prospects. Advanced Materials, 26(27), 4607-4626 (2014).
- [8] X. Chen, C. Li, M. Grätzel, R. Kostecki, & S. S. Mao. Nanomaterials for renewable energy production and storage. Chemical Society Reviews, 41(23), 7909-7937 (2012).
- [9] A. A. Adewale, A. Chik, T. Adam, O. K. Yusuff, S. A. Ayinde, & Y. K. Sanusi. First principles calculations of structural, electronic, mechanical and thermoelectric properties of cubic ATiO3 (A= Be, Mg, Ca, Sr and Ba) perovskite oxide., Computational Condensed Matter, 28, e00562 (2021).
- [10] S. Dahbi, N. Tahiri, O. El Bounagui, & H. Ez-Zahraouy. Electronic, optical, and thermoelectric properties of perovskite BaTiO3 compound under the effect of compressive strain. Chemical Physics, 544, 111105 (2021).
- [11] N. Tahiri, S. Dahbi, I. Dani, O. El Bounagui, & H. Ez-Zahraouy. Magnetocaloric and thermoelectric properties of the perovskite LaMnO3 material: a DFT study and Monte Carlo technique. Phase Transitions, 94(11), 826-834 (2021).
- [12] S. Feng, P. Zhang, Y. Zhang, J. Cao, Y. Zheng, J. Wang, L Shi, J Pan, & C. Li. Self-cleaning transparent photovoltaic device in perovskite SrTiO3 quantum dot modified CuGaO2/Zn2SnO4 nanoarrays pn junction via surface plasma modification., Applied Physics Letters, 125(9) (2024).
- [13] A. Koufi, Y. Ziat & H. Belkhanchi. Study of the Gravimetric, Electronic and Thermoelectric Properties of XAlH3 (X = Be, Na, K) as hydrogen storage perovskite using DFT and the BoltzTrap Software Package. Solar Energy and Sustainable Development, 53–66 (2024). https://doi.org/10.51646/jsesd.v14iSI MSMS2E.403.
- [14] H. S. Magar, A. M. Mansour, & A. B. A. Hammad. Advancing energy storage and supercapacitor applications through the development of Li+-doped MgTiO3 perovskite nanoceramics. Scientific Reports, 14(1), 1849 (2024).
- [15] T. A. Otitoju, P. U. Okoye, G. Chen, Y. Li, M. O. Okoye, & S. Li. Advanced ceramic

- components: Materials, fabrication, and applications. Journal of industrial and engineering chemistry, 85, 34-65 (2020).
- [16] M. Passi, & B. Pal. A review on CaTiO3 photocatalyst: Activity enhancement methods and photocatalytic applications. Powder Technology, 388, 274-304 (2021).
- [17] Q. Zhang, Y. Wang, Y. Jia, W. Yan, Q. Li, J. Zhou, & K. Wu. Engineering the Electronic Structure towards Visible Lights Photocatalysis of CaTiO3 Perovskites by Cation (La/Ce)-Anion (N/S) Co-Doping: A First-Principles Study., Molecules, 28(20), 7134 (2023).
- [18] D. K. Bhat, H. Bantawal, P. I. Uma, S. P. Kumar & U. S. Shenoy. Designing sustainable porous graphene-CaTiO3 nanocomposite for environmental remediation. Sustainable Chemistry for the Environment, 5, 100071 (2024).
- [19] A. Krause, W. M. Weber, D. Pohl, B. Rellinghaus, A. Kersch & T. Mikolajick. Investigation of band gap and permittivity of the perovskite CaTiO3 in ultrathin layers. Journal of Physics D: Applied Physics, 48(41), 415304 (2015).
- [20] X. J. Huang, Y. A. N. Xin, H. Y. Wu, F. A. N. G. Ying, Y. H. Min, W. S. Li, S. Y. Wang & Z. J. Wu. Preparation of Zr-doped CaTiO3 with enhanced charge separation efficiency and photocatalytic activity., Transactions of Nonferrous Metals Society of China, 26(2), 464-471 (2016).
- [21] M. Rizwan, Z. Usman, M. Shakil, S. S. A. Gillani, S. Azeem, H. B. Jin, C. B. Cao, R. F. Mehmood, G. Nabi & M. A. Asghar. Electronic and optical behaviour of lanthanum doped CaTiO3 perovskite. Materials Research Express, 7(1), 015920 (2020).
- [22] I. Grinberg, D. V. West, M. Torres, G. Gou, D. M. Stein, L. Wu, G. Chen, E. M. Gallo, A. R. Akbashev, P. K. Davies, J. E. Spanier & A. M. Rappe. Perovskite oxides for visible-light-absorbing ferroelectric and photovoltaic materials. Nature,, 503(7477), 509-512 (2013).
- [23] H. Liu, J. Cheng, H. Dong, J. Feng, B. Pang, Z. Tian, S. Ma, F. Xia, C. Zhang & L. Dong. Screening stable and metastable ABO3 perovskites using machine learning and the materials project. Computational Materials Science, 177, 109614 (2020).
- [24] L. Attou, A. Al-Shami, J. Boujemaâ, O. Mounkachi, & H. Ez-Zahraouy. Predicting the structural, optoelectronic, dynamical stability and transport properties of Boron-doped CaTiO3: DFT based study. Physica Scripta, 97(11), 115808 (2022).
- [25] S. Chahar, K. K. Mishra, & R. Sharma. Analysing the suitability of CaTiO3/Ca1-xSrxTiO3/SrTiO3 perovskite for fabrication of optoelectronic devices using QuantumATK tool: a study for electronic and optical properties., Physica Scripta, 99(3), 035963 (2024).
- [26] P. Blaha, K. Schwarz, G. K. Madsen, D. Kvasnicka & J. Luitz. wien2k. An augmented plane wave+ local orbitals program for calculating crystal properties, 60(1) (2001).
- [27] M. Miri, Y. Ziat, H. Belkhanchi, & Y. A. El Kadi. Structural, elastic, and opto-electronic conduct of half Heusler Li (Ca, Mg, Zn) N alloys: Ab initio computation. Solid State Communications, 396, 115765 (2025). https://doi.org/10.1016/j.ssc.2024.115765
- [28] D. Koller, F. Tran, & P. Blaha. Improving the modified Becke-Johnson exchange potential. Physical Review B—Condensed Matter and Materials Physics, 85(15), 155109 (2012).
- [29] V. K. Solet, & S. K. Pandey. Assessing the performance of Mg $\ _{2} \$ Si and Ca $\ _{2} \$ Si from DFT and SLME calculations for solar cell applications. arXiv preprint arXiv:2401.05296 (2024).
- [30] F. D. Murnaghan. The compressibility of media under extreme pressures. Proceedings of the National Academy of Sciences, 30(9), 244-247 (1944).

- [31] P. H. Mott, J. R. Dorgan & C. M. Roland. The bulk modulus and Poisson's ratio of "incompressible" materials. Journal of Sound and Vibration, 312(4-5), 572-575 (2008).
- [32] R. Ali, & M. Yashima. Space group and crystal structure of the perovskite CaTiO3 from 296 to 1720 K. Journal of Solid State Chemistry, 178(9), 2867-2872 (2005).
- [33] B. J. Kennedy, C. J. Howard, & B. C. Chakoumakos. Phase transitions in perovskite at elevated temperatures-a powder neutron diffraction study. Journal of Physics: Condensed Matter, 11(6), 1479 (1999).
- [34] Q. Mahmood, M. Yaseen, B. U. Haq, A. Laref, & A. Nazir. The study of mechanical and thermoelectric behavior of MgXO3 (X= Si, Ge, Sn) for energy applications by DFT. Chemical Physics, 524, 106-112 (2019).
- [35] H. Fatihi, M. Agouri, H. Ouhenou, H. Benaali, A. Zaghrane, A. Abbassi, M. El Idrissi, S. Taj & B. Manaut. Enhancing Solar Cell Efficiency: A Comparative Study of Lead-Free Double Halide Perovskites \$\$ Rb_{2} CuAsBr_{6} \$\$ and, \$\$ Rb_{2} TlAsBr_{6} \$\$ using DFT and SLME Methods. Journal of Inorganic and Organometallic Polymers and Materials, 1-14 (2024).
- [36] A. Bouzaid, Y. Ziat, H. Belkhanchi, H. Hamdani, A. Koufi, M. Miri, C. Laghlimi, Z. Zarhri. Ab initio study of the structural, electronic, and optical properties of MgTiO3 perovskite materials doped with N and P. E3S Web of Conferences, (Vol. 582, p. 02006), (2024) https://doi.org/10.1051/e3sconf/202458202006
- [37] X. Zhou, J. Shi, & C. Li. Effect of metal doping on electronic structure and visible light absorption of SrTiO3 and NaTaO3 (Metal= Mn, Fe, and Co). The Journal of Physical Chemistry C, 115(16), 8305-8311. 2011.
- [38] H. Bentour, M. Boujnah, M. Houmad, M. El Yadari, A. Benyoussef, & A. El Kenz. DFT study of Se and Te doped SrTiO 3 for enhanced visible-light driven phtocatalytic hydrogen production. Optical and Quantum Electronics, 53, 1-13. 2021..
- [39] D. E. Vanpoucke, P. Bultinck, S. Cottenier, V. Van Speybroeck, & I. Van Driessche. Aliovalent doping of CeO₂: DFT study of oxidation state and vacancy effects. (2014).
- [40] Q. Zhang, Y. Wang, Y. Jia, W. Yan, Q. Li, J. Zhou, & K. Wu. Engineering the Electronic Structure towards Visible Lights Photocatalysis of CaTiO3 Perovskites by Cation (La/Ce)-Anion (N/S) Co-Doping: A First-Principles Study., Molecules, 28(20), 7134 (2023).
- [41] A. Bouzaid, Y. Ziat, H. Belkhanchi. Prediction the effect of (S, Se, Te) doped MgTiO3 on optoelectronic, catalytic, and pH conduct as promised candidate photovoltaic device: Ab initio framework. International Journal of Hydrogen Energy,, 100, 20-32 (2025) https://doi.org/10.1016/j.ijhydene.2024.12.284
- [42] U. Balachandran, B. Odekirk, & N. G. Eror. Electrical conductivity in calcium titanate. Journal of Solid State Chemistry, 41(2), 185-194. 1982..
- [43] Y. Ziat, H. Belkhanchi & Z. Zarhri. DFT Analysis of Structural, Electrical, and Optical Properties of S, Si, and F-Doped GeO2 Rutile: Implications for UV-Transparent Conductors and Photodetection. Solar Energy and Sustainable Development, 14(1), 74–89 (2025). https://doi.org/10.51646/jsesd.v14i1.232.
- [44] R. Majumder, M. M. Hossain, & D. Shen. First-principles study of structural, electronic, elastic, thermodynamic and optical properties of LuPdBi half-Heusler compound. Modern Physics Letters B, 33(30), 1950378 (2019).
- [45] Y. Ziat, Z. Zarhri, H. Belkhanchi, O. Ifguis, A. D. Cano. Effect of Be and P doping on the electron density, electrical and optoelectronic conduct of half-Heusler LiMgN within ab initio scheme. Physica Scripta, 97(10), 105802 (2022). https://iopscience.iop.org/article/10.1088/1402-4896/

ac8b40/meta

- [46] L. De, R. Kronig. On the theory of dispersion of x-rays. Journal of the Optical Society of America, 12(6), 547-557 (1926).
- [47] J. S. Toll. Causality and the dispersion relation: logical foundations. Physical review, 104(6), 1760 (1956).
- [48] C. M. Okoye. Theoretical study of the electronic structure, chemical bonding and optical properties of KNbO3 in the paraelectric cubic phase. Journal of Physics: Condensed Matter, 15(35), 5945 (2003).
- [49] C. Ambrosch-Draxl, & R. Abt. The calculation of optical properties within WIEN97. ICTP Lecture Notes. (1998).
- [50] M. Kumar, R. P. Singh, & A. Kumar. Opto-electronic properties of HfO2: a first principle-based spin-polarized calculations. Optik, 226, 165937 (2021).
- [51] S. Saha, T. P. Sinha, & A. Mookerjee. Electronic structure, chemical bonding, and optical properties of paraelectric BaTiO 3. Physical Review B, 62(13), 8828 (2000).
- [52] M. Miri, Y. Ziat, H. Belkhanchi, Z. Zarhri, Y. A. El Kadi. Structural and optoelectronic properties of LiYP (Y= Ca, Mg, and Zn) half-Heusler alloy under pressure: A DFT study. Physica B: Condensed Matter, 667, 415216 (2023). https://doi.org/10.1016/j.physb.2023.415216
- [53] A. Delin, O. Eriksson, R. Ahuja, B. Johansson, M. S. S. Brooks, T. Gasche, S. Auluck & J. M. Wills. Optical properties of the group-IVB refractory metal compounds. Physical Review B, 54(3), 1673 (1996).
- [54] M. Rizwan, A. Ayub, M. Shakil, Z. Usman, S. S. A. Gillani, H. B. Jin, & C. B. Cao. Putting DFT to trial: For the exploration to correlate structural, electronic and optical properties of M-doped (M= Group I, II, III, XII, XVI), lead free high piezoelectric c-BiAlO3. Materials Science and Engineering: B, 264, 114959 (2021).
- [55] E. Zahedi, M. Hojamberdiev, & M. F. Bekheet. Electronic, optical and photocatalytic properties of three-layer perovskite Dion–Jacobson phase CsBa 2 M 3 O 10 (M= Ta, Nb): a DFT study., Rsc Advances, 5(108), 88725-88735 (2015).
- [56] S. Dahbi, N. Tahiri, O. El Bounagui, & H. Ez-Zahraouy. The new eco-friendly lead-free zirconate perovskites doped with chalcogens for solar cells: Ab initio calculations. Optical Materials, 109, 110442 (2020).
- [57] B. Mouhib, S. Dahbi, A. Douayar, N. Tahiri, O. El Bounagui, & H. Ez-Zahraouy. Theoretical investigations of electronic structure and optical properties of S, Se or Te doped perovskite ATiO3 (A= Ca, Ba, and Sr) materials for eco-friendly, solar cells. Micro and Nanostructures, 163, 107124 (2022).
- [58] A. Ilyas, S. A. Khan, K. Liaqat, & T. Usman. Investigation of the structural, electronic, magnetic, and optical properties of CsXO3 (X= Ge, Sn, Pb) perovskites: A first-principles calculations. Optik, 244, 167536., (2021).